forum acusticum 2026
8-12 September · Graz, Austria

AUTOMATED DESIGN METHOD FOR VENTILATED CUBE-SHAPED ACOUSTIC METAMATERIALS IN SOUND TRANSMISSION LOSS APPLICATIONS

Emilia Żak-Stefanowska[1, 2], Adam Pilch[1], Janina Krzysiak[2]

[1] *AGH University of Krakow, Krakow, Poland*
[2] *Hitachi Energy Research, Krakow, Poland*

This paper is a revised version of the authors' submitted manuscript that was peer-reviewed by at least two anonymous reviewers.

Abstract

The growing use of design methods based on machine learning and optimization has increased the need for methods capable of generating large, high-quality acoustics datasets. To address this, we present a stochastic 3D geometry generation algorithm for irregular, ventilated acoustic metamaterials that support resonant behavior in sound transmission loss applications. The method operates on a voxel grid, using a flood-growth rule with lateral expansion and inter-layer propagation to synthesize fully connected air duct networks. Finite element simulation model used for the analysis of the generated geometries is validated experimentally using ten cube-structured geometries fabricated as laser-cut birch plywood specimens. Validation employs four-microphone transmission loss measurements in an impedance tube over 500–6400 Hz. Across all designs, the numerical model reproduces experiments with an average absolute discrepancy of 2.3 dB, standard deviation of 1.4 dB, and maximum of 11.8 dB. Although no specific optimization was targeted, some samples already show a promising broadband transmission loss, reaching up to 58 dB at 2650 Hz. Overall, the proposed method provides a validated foundation for data-driven design of ventilated metamaterials.

Keywords: *acoustic metamaterials, design, sound transmission loss, impedance tube*

1. Introduction

Rising noise levels in modern environments have driven the need for compact, robust, and highly efficient sound attenuation solutions. Acoustic metamaterials (AMs) have emerged as a promising approach to meet this demand [1]. These engineered structures are designed so that their geometry controls effective properties such as mass density and bulk modulus, reducing reliance on constituent material properties. The distinctive acoustic behavior of AMs typically arises from the collective response of local resonators [2].

Moreover, compared to conventional materials, AMs offer several key advantages in practical applications: they can be fabricated from stiff and durable materials instead of delicate porous media and they enable compact designs with ventilation capabilities, unlike traditional rigid barriers or enclosures. Since many industrial noise sources are heat-generating machines that require both effective sound attenuation and adequate cooling, AMs are particularly attractive for such applications.

Numerous resonant AM concepts have been proposed, including designs based on Helmholtz resonators, coiled channels [3], membrane-type elements [4], and fractal cavities [5], many of which achieve high sound transmission loss (STL) or absorption in targeted bands while remaining compact. However, AM geometry design still largely relies on manual tuning and human intuition [6], with many configurations based on assemblies of resonant unit cells that offer only relatively narrowband performance. Although some studies have explored complex three-dimensional geometries [6], [7], this area remains underexplored, especially for ventilated AMs targeting high STL. Existing optimization approaches are often restricted to two-dimensional or symmetric layouts, which might limit the development of more complex structures, capable of broadband attenuation. Designing AMs with irregular 3D air paths for broadband attenuation can be therefore challenging. Meanwhile, emerging data-driven and machine learning approaches that could assist with such tasks typically require large, diverse datasets generated using numerical models.

This underscores the need for automatic 3D geometry generation frameworks that: (i) generate complex,

Corresponding author: *stefanowska@agh.edu.pl.*

parametrized geometries that support rich resonant behavior, (ii) enforce air-permeability constraints, (iii) produce manufacturable geometries, and (iv) are supported by numerical models that have been experimentally validated, to support further data-driven optimization.

This study addresses these challenges by introducing a constrained 3D stochastic geometry generation framework for layered, resonant AMs designed for STL applications. The geometry is defined on a voxel grid and constructed using a recursive flood growth rule with probabilistic lateral expansion and layer to layer propagation, ensuring continuous air paths between inlet and outlet while enabling a rich family of irregular air duct networks. The framework thus satisfies connectivity constraints and produces complex, yet manufacturable, parametrized geometries. We demonstrate the sound attenuation capabilities of the geometries generated with the proposed method using finite element method (FEM) simulations in COMSOL Multiphysics and experimental STL measurements in an impedance tube.

The main contributions of this paper are as follows:

- We introduce a stochastic generation algorithm for 3D cube-structured AM air ducts that guarantees a continuous airflow path while allowing irregular internal geometries;
- We propose a layered manufacturing strategy of generated structures based on laser-cut plywood;
- We propose a supporting FEM model for STL calculation, which we validate experimentally on a subset of geometries using impedance tube measurements.

The proposed framework, although does not showcase optimized geometries, could serve as a good foundation for further data-driven dataset generation.

The remainder of the paper is structured as follows: Section 2 describes the geometry generation algorithm, the numerical model, the manufacturing process and the experimental setup. Section 3 presents representative STL results from simulations and measurements, followed by a discussion in Section 4 and conclusions in Section 5.

2. Methodology

2.1. Air duct geometry design

The geometry of the metamaterial air duct is defined within a discretized bounded three-dimensional design domain, arranged into a grid of $N_x \times N_y \times N_z$ voxels, where each voxel corresponds to a cuboid with side lengths d_x, d_y, d_z, as presented in Figure 1. The maximum air duct volume is $(N_x \cdot d_x) \times (N_y \cdot d_y) \times (N_z \cdot d_z)$, with the acoustic propagation direction aligned with the z-axis, i.e., sound travels through the stack of layers from the inlet face at $z = 1$ to the outlet face at the last layer $z = N_z \cdot d_z$.

For each specimen, the air duct geometry is generated sequentially according to Algorithm 1. Each voxel is

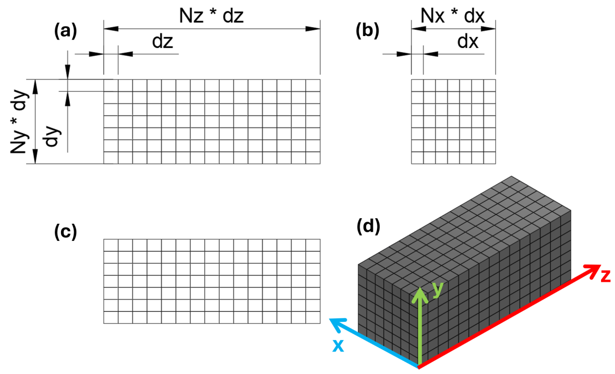

Figure 1: Design domain of the AM air ducts shown in four views: (a) top, (b) front, (c) side, and (d) 3D.

assigned one of two states: solid (value 0), representing a structural material, or void (value 1), representing an air-filled region. The algorithm generates a connected 3D air duct network by growing void voxels set layer by layer from a prescribed inlet seed.

In each layer, the lateral expansion is performed first. Starting from the current front of air voxels, in-plane neighbors are visited, stochastically converted from solid to air with a given lateral probability $p_{\text{lat}} \in [0, 1]$. The in-plane neighbors of a voxel (x, y, z) are its four face-adjacent neighbours within the same layer, i.e., $(x \pm 1, y, z)$ and $(x, y \pm 1, z)$ that remain inside the design domain. After completion of the in-plane lateral propagation, the algorithm performs forward propagation to the next layer, where each air voxel in the current layer is stochastically extended in the propagation direction with a forward propagation probability $p_{\text{forw}} \in [0, 1]$. If no voxel advances, at least one is forced to continue, which guarantees a continuous path from the inlet to the outlet through the voxel grid. Generated geometries can be effectively represented using binary bitmap formats, enabling straightforward parameterization and optimization.

For this study, we generated geometries using parameters $N_x = 7$, $N_y = 7$, $N_z = 15$, $d_x = d_y = 2.5\,\text{mm}$, $d_z = 3.0\,\text{mm}$, $p_{\text{lat}} = 0.3$, and $p_{\text{forw}} = 0.2$. The geometric parameters were selected to balance practical fabrication accuracy with enough geometric complexity. The probability values were then tuned heuristically to obtain a suitable balance between air and solid regions.

We selected ten samples from a pool of 5,000 candidates screened in preliminary numerical simulations with 1/3-octave band resolution, using a model before experimental data tuning. The chosen samples (ID:01–ID:10) comprise the strongest STL performers (by peak and mean STL) and the weakest (by mean STL) from this initial assessment. Figures 2 and 3 illustrate the air duct geometries for two representative cases.

2.2. Manufacturing of samples

Although additive manufacturing is widely used for AM prototyping [8], the geometry generation algo-

Algorithm 1: Stochastic 3D voxel-based air duct generation for AMs

Input: **Grid**: domain Ω of size (N_x, N_y, N_z) voxels indexed (x, y, z) for $x = 1, \ldots, N_x$, $y = 1, \ldots, N_y$, $z = 1, \ldots, N_z$; **Inlet**: voxel $A_0 = (x_1, y_1, 1)$, where (x_1, y_1) is the chosen inlet voxel in the $z = 1$ plane; **Probabilities of expansion**: lateral p_{lat} and forward p_{forw}.

Output: Voxel state field $S(x, y, z) \in \{0, 1\}$, where $S = 0$ denotes air and $S = 1$ denotes solid.

Initialization: Set $S(x, y, z) \leftarrow 1$ for all x, y, z; set $S(x_1, y_1, 1) \leftarrow 0$.

for $z = 1$ **to** $N_z - 1$ **do**
  // Lateral expansion in layer z
  $\mathcal{F} \leftarrow \{(x, y) \mid S(x, y, z) = 0\}$;
  while $\mathcal{F} \neq \emptyset$ **do**
    Select $(x, y) \in \mathcal{F}$ and remove it from $\mathcal{F}$;
    foreach *in-plane neighbour* (x', y') *of* (x, y) *within bounds* **do**
      Draw $u \sim \mathcal{U}(0, 1)$;
      if $u < p_{\text{lat}}$ ***and*** $S(x', y', z) = 1$ **then**
        $S(x', y', z) \leftarrow 0$; add (x', y') to $\mathcal{F}$;
  // Forward propagation to layer $z + 1$
  $\mathcal{L}_z \leftarrow \{(x, y) \mid S(x, y, z) = 0\}$, $\mathcal{F}_{z+1} \leftarrow \emptyset$;
  foreach $(x, y) \in \mathcal{L}_z$ **do**
    Draw $u \sim \mathcal{U}(0, 1)$;
    if $u < p_{\text{forw}}$ ***and*** $S(x, y, z + 1) = 1$ **then**
      $S(x, y, z + 1) \leftarrow 0$; add (x, y) to $\mathcal{F}_{z+1}$;
  if $\mathcal{F}_{z+1} = \emptyset$ **then**
    Select $(x, y) \in \mathcal{L}_z$; $S(x, y, z + 1) \leftarrow 0$; add (x, y) to $\mathcal{F}_{z+1}$;

return $S(x, y, z)$;

rithm described in Section 2.1 also enables an alternative layered fabrication route that uses plywood as the base material. This choice provides benefits such as higher stiffness, lower porosity, and easier structural scalability, at the cost of stricter limits on minimum feature size, tighter fabrication tolerances, and more labor-intensive manufacturing. For the experimental validation, we produced plywood samples with a target outer diameter of 29 mm, matching the inner diameter of the impedance tube described in Section 2.4.

To manufacture the experimental samples, each voxel-based layer was converted into a two-dimensional pattern and cut from a 3 mm birch plywood using a laser plotter, yielding 15 individual disks per specimen. To ensure accurate inter-layer positioning, each disk incorporated two alignment tabs that engaged with a custom alignment guide during assembly. The layers were then bonded with wood glue based on

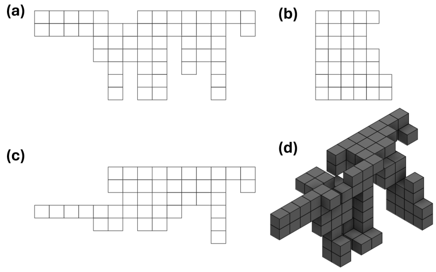

Figure 2: Example of the generated geometry - air duct shape of sample ID:01 shown in four views: (a) top, (b) front, (c) side, and (d) 3D.

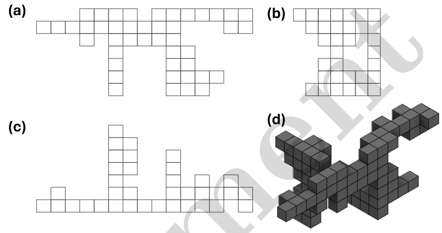

Figure 3: Example of the generated geometry - air duct shape of sample ID:04 shown in four views: (a) top, (b) front, (c) side, and (d) 3D.

polyvinyl acetate (PVA) to form cylindrical stacks. The assembled stacks were produced slightly oversize and subsequently machined to their final dimensions on a lathe, achieving the 29 mm diameter required for a precise fit in the impedance tube. Photographs of the process are shown in Figures 4 and 5.

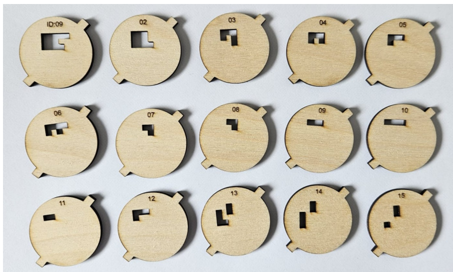

Figure 4: Manufacturing of AM samples - individual layers before assembly for sample ID:09.

2.3. Numerical simulation

The acoustic performance of the generated geometries was analyzed using FEM simulation. The numerical model was designed to closely resemble the experimental measurements in the impedance tube setup. The model settings were prepared according to the COMSOL Acoustic Module User's Guide [9].

The acoustic field was modeled using the Pressure Acoustics, Frequency Domain interface, with the plywood–air boundary represented by an Impedance condition using the Porous layer option and the Delany–Bazley model, with flow resistivity $R_f = 10^7\ \text{Pa} \cdot \text{s/m}^2$ fitted once across all ten specimens by

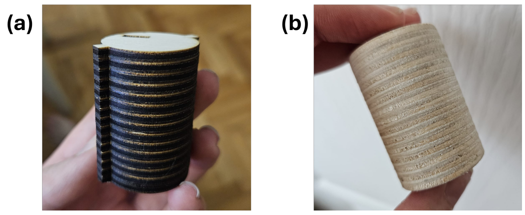

Figure 5: Manufacturing of AM samples: (a) layers after assembly, but before lathe processing; (b) after lathe processing.

minimizing the mean absolute STL error, and held fixed thereafter. The plywood is assumed to be acoustically rigid and the porous layer is intended to represent surface roughness rather than a physical porous layer. This modeling strategy was selected after comparing several boundary-condition combinations during model development, including full multiphysics with the plywood explicitly modeled as a solid domain. The Delany–Bazley approach reproduced the experimental results faithfully at substantially lower computational cost compared to full multiphysics simulation.

Plane-wave excitation was implemented via the ports interface at the inlet and outlet cross-sections, enabling direct computation of STL from the complex pressure fields. The amplitude of the plane wave was set to $A = 1\,\mathrm{Pa}$.

The computational mesh followed COMSOL and literature recommendations [9], [10]. Rectangular elements were used in the air duct channels, while tetrahedral elements were used elsewhere. Additionally, boundary-layer elements were included at the air duct walls to ensure appropriate calculations of thermoviscous effects. Maximum mesh element size was globally set to $\lambda_{\min}/6$, where $\lambda_{\min}$ is the shortest wavelength of the analyzed frequency range. A representative example of used meshing is shown in Figure 6 with zoom-in on detail for boundary layers in Figure 7. For this study, simulations were conducted in the range of 500–6400 Hz to match the experimental measurement setup described in Section 2.4.

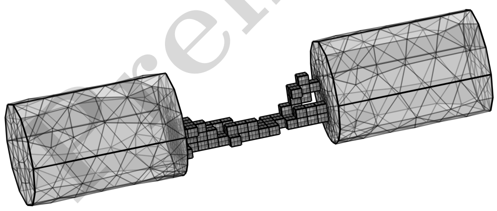

Figure 6: FEM simulation meshing for sample ID:09.

The computational cost of numerical simulations increases with the number of degrees of freedom, which in turn grows with the number of mesh elements. Consequently, the computation time depends on the number of air voxels within the air-duct geometry, i.e., more elements result in longer simulation times. In the geometries analyzed in this study, the num-

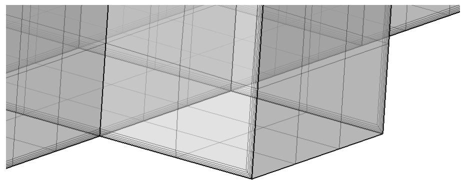

Figure 7: FEM simulation meshing for sample ID:09 - boundary layers.

ber of degrees of freedom ranged from approximately 10,000 to 180,000. All simulations were performed on a laptop equipped with an Intel(R) Core(TM) Ultra 9 275HX processor (2.70 GHz) and 64 GB of RAM. On this machine, the computation of a single frequency point required on average 1.42 s. This implies that generating a numerical dataset at 12 frequency points (for example, 1/3-octave bands in range 500–6300 Hz) for 10,000 geometries would require nearly 50 hours of computation.

2.4. Experimental measurement setup

STL measurements were performed in a Brüel and Kjær Transmission Loss Tube Kit Type 4206-T (500–6400 Hz) equipped with four ¼" pressure-field microphones. The setup followed the manufacturer's instructions for the four-microphone transfer-function method [11], in accordance with the ASTM E2611-19 transfer-matrix test method [12]. The microphones were calibrated before each measurement session using a Sound Calibrator Type 4231, and consequently phase calibration was performed within the PULSE impedance tube software. The experimental setup is presented in Figure 8.

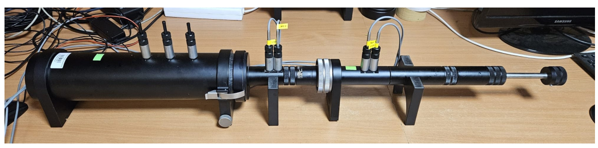

Figure 8: Experimental setup.

Each sample was mounted in the transmission loss sample holder using a thin layer of vaseline to ensure an airtight seal. For each specimen, three repeated measurements were performed under both rigid and anechoic termination conditions. Subsequently, the transfer functions and STL characteristics were computed across the 500–6400 Hz frequency range with a resolution of 4 Hz. The employed mounting procedure resulted in highly repeatable STL values. Across the ten tested sample geometries in experimental results, the average standard deviation among the three repetitions was 0.53 dB, with a maximum of 4.6 dB. The deviations were especially prominent for higher frequencies, which is an expected outcome, most likely due to the shorter wavelengths of the waves. A representative result is shown in Figure 9. For further results in Section 3, experimental results are taken as the average STL of three successive measurements of the same sample.

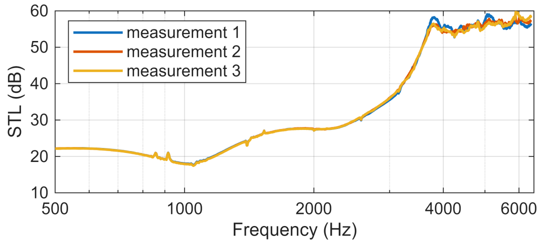

Figure 9: Experimental results for sample ID:05.

3. Results

The comparison between simulated and measured STL for representative voxel-generated geometries is shown in Figure 10. We report results for a sample with the highest measured mean STL (42.7 dB for ID:01), one with the highest measured peak STL (58.0 dB at 2650 Hz for ID:04) and a sample with the lowest mean STL (18.3 dB for ID:09). The simulated STL curves reproduce the main trends observed experimentally, which indicates that the FEM model provides a reasonably accurate prediction of the structures STL within the investigated frequency range.

Beyond visual inspection, the agreement between simulations and measurements was quantified over the full frequency range for all ten samples. We evaluated the mean absolute STL difference between numerical and experimental data, its standard deviation, and the maximum point-wise STL deviation. The average absolute STL error was 2.3 dB, with a standard deviation of 1.4 dB. The maximum deviation at any single frequency point did not exceed 11.8 dB. The maximum deviation was found for sample ID:01 at 3450 Hz and is presented in Figure 10(a).

The results further show that the stochastic voxel-based generator does not exclusively produce geometries with high STL. Several tested designs exhibit more moderate attenuation levels. This behavior is consistent with the intended role of the algorithm as a flexible geometry generator rather than an optimization scheme targeting maximum STL. The demonstrated agreement between simulations and measurements for a subset of samples suggests that the validated numerical model could, in future work, support automated FEM-based data generation at larger scale.

Additionally, inspection of the simulated sound pressure level distributions at selected frequencies reveals localized pressure extrema within individual cavities, consistent with resonant behavior of the internal air volumes (see example in Figure 11). This qualitative agreement between the expected cavity resonances and the numerically predicted field distributions provides further evidence that the FEM model captures the dominant acoustic mechanisms governing the measured STL response.

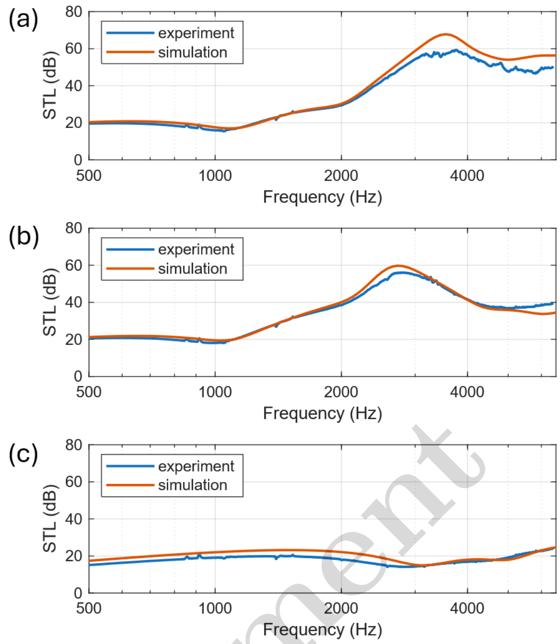

Figure 10: STL results of generated geometries: (a) ID:01, (b) ID:04, (c) ID:09.

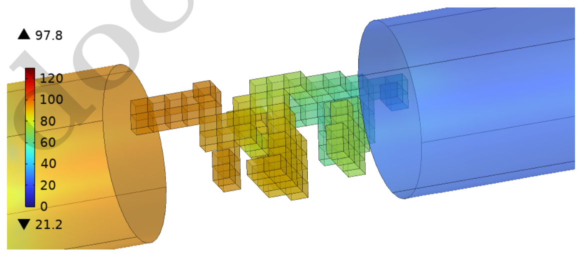

Figure 11: Sound pressure level in decibels at 3450 Hz for geometry ID:01.

4. Discussion

The proposed framework offers several advantages but also reveals directions for future work. The geometry generation algorithm allows the automatic creation of a vast array of irregular, fully connected 3D air path topologies that support acoustic resonance. The STL analysis indicates that such geometries can provide broadband attenuation, in contrast to the mainly peak-dominated responses reported in e.g., [3] and [13]. The numerical model reproduces the main experimental features with good accuracy, validating the layered plywood fabrication route as a practical tool for the design of ventilated acoustic metamaterials.

Next, the 3D geometry generator might enable production of large datasets of structurally diverse air-duct configurations for training machine learning models. For example, computing 12 frequency points for 10,000 geometries is estimated to require roughly 50 hours of simulation time, which represents a reasonable computational effort for this type of task.

Another advantage is the layered manufacturing strategy, which allows realizing the structures in laser-cut plywood instead of additive manufacturing materials. In enclosure-type products, repeating a single air-duct pattern across a wall or panel could eliminate the need for cylindrical machining and lathe post-processing.

The present implementation also has several limitations. Using binary voxels simplifies encoding but restricts channel cross-sections to a coarse grid. Extending the framework to continuous or multilevel parameterizations could offer finer geometric control. In addition, although the generated structures maintain open air paths and thus, in principle, permit airflow, the present study does not quantify pressure drop or ventilation performance. A follow up study should treat airflow metrics as additional design objectives and experimental observables.

Finally, the current prototypes operate in a relatively high frequency range. However, the proposed methodology allows control of the operating band via the chosen voxel dimensions. Geometric upscaling of the design could be therefore further used to target lower-frequency noise control.

Taken together, these results suggest that the proposed method might provide a pathway toward data-driven design of ventilated acoustic metamaterials. The framework already delivers some geometries with promising broadband STL performance in relatively compact samples and could naturally extend to optimization or machine learning workflows.

5. Conclusions

This study introduced a stochastic voxel-based framework for generating layered, cube-structured acoustic metamaterials with air permeability. The proposed approach enables fully automatic synthesis of complex, parametrized networks of air paths. The accompanying numerical model was validated against impedance tube measurements on ten geometries fabricated as laser-cut layered birch plywood specimens. Within the explored parameter range, the numerical and experimental STL results show consistency and indicate that the proposed method could be used for further design approaches based on optimization or machine learning.

Acknowledgments

The authors gratefully acknowledge PhD Rafal Kudelski for invaluable assistance with lathe machining of the plywood samples.

References

[1] G. Liao, C. Luan, Z. Wang, J. Liu, X. Yao, and J. Fu, "Acoustic Metamaterials: A Review of Theories, Structures, Fabrication Approaches, and Applications," en, *Advanced Materials Technologies*, vol. 6, no. 5, p. 2 000 787, May 2021. DOI: 10.1002/admt.202000787.

[2] W. S. Gan, *New Acoustics Based on Metamaterials* (Engineering Materials), eng. Singapore: Springer Singapore, 2018. DOI: 10.1007/978-981-10-6376-3.

[3] Z. Xiao, P. Gao, D. Wang, X. He, and L. Wu, "Ventilated metamaterials for broadband sound insulation and tunable transmission at low frequency," en, *Extreme Mechanics Letters*, vol. 46, p. 101 348, Jul. 2021. DOI: 10.1016/j.eml.2021.101348.

[4] F. Ma, C. Wang, C. Liu, and J. H. Wu, "Structural designs, principles, and applications of thin-walled membrane and plate-type acoustic/elastic metamaterials," en, *Journal of Applied Physics*, vol. 129, no. 23, p. 231 103, Jun. 2021. DOI: 10.1063/5.0042132.

[5] G. Comandini, M. Ouisse, V. P. Ting, and F. Scarpa, "Acoustic transmission loss in hilbert fractal metamaterials," en, *Scientific Reports*, vol. 13, no. 1, p. 19 058, Nov. 2023. DOI: 10.1038/s41598-023-43646-1.

[6] R. Karimi Mahabadi et al., "Graph-based design of irregular metamaterials," en, *International Journal of Mechanical Sciences*, vol. 295, p. 110 203, Jun. 2025. DOI: 10.1016/j.ijmecsci.2025.110203.

[7] X. Yang et al., "Multilayer stackable grouped acoustic metamaterial with optional sound absorption performance," en, *Journal of Applied Physics*, vol. 137, no. 12, p. 123 104, Mar. 2025. DOI: 10.1063/5.0254856.

[8] M. Askari et al., "Additive manufacturing of metamaterials: A review," en, *Additive Manufacturing*, vol. 36, p. 101 562, Dec. 2020. DOI: 10.1016/j.addma.2020.101562.

[9] *Acoustic Module User's Guide. COMSOL Multiphysics® v. 6.3. COMSOL AB, Stockholm, Sweden. 2025.*

[10] N. Jiménez, O. Umnova, and J.-P. Groby, Eds., *Acoustic Waves in Periodic Structures, Metamaterials, and Porous Media: From Fundamentals to Industrial Applications* (Topics in Applied Physics), en. Cham: Springer International Publishing, 2021, vol. 143. DOI: 10.1007/978-3-030-84300-7.

[11] Brüel & Kjær, *Product data for Impedance Tube Kit (50 Hz– 6.4 kHz) Type 4206, Impedance Tube Kit (100 Hz– 3.2 kHz) Type 4206-A and Transmission Loss Tube Kit (50 Hz– 6.4 kHz) Type 4206-T.*

[12] E33 Committee, *Test Method for Normal Incidence Determination of Porous Material Acoustical Properties Based on the Transfer Matrix Method*, en. DOI: 10.1520/E2611-19.

[13] X.-L. Gai et al., "Acoustic properties of honeycomb like sandwich acoustic metamaterials," en, *Applied Acoustics*, vol. 199, p. 109 016, Oct. 2022. DOI: 10.1016/j.apacoust.2022.109016.